Institute of Energy Plant Technology,

Ruhr-University Bochum,

Documentation of the user-defined functions (UDFs) for simulating the conversion behaviour of refuse-derived-fuel (RDF) within the ANSYS Fluent® framework

Contents

1 Models for describing the combustion and flight behaviour of RDF

The following section describes the physical/chemical principles of the FLUENT UDFs used to describe the thermochemical conversion of RDF, which were developed by the Institute of Energy Plant Technology. For the standard fuel coal dust, in case it is co-fired, the standard routines provided by FLUENT are used.

1.1.1 Characterization of RDF

RDF is characterized by an irregular particle shape with a complex form. The modeling approach chosen for the burning and flight behaviour is based on an approximation of the complex, often flat particle geometry using a cuboid body with three defined edge lengths a, b, and c, as shown in Figure 1.1.

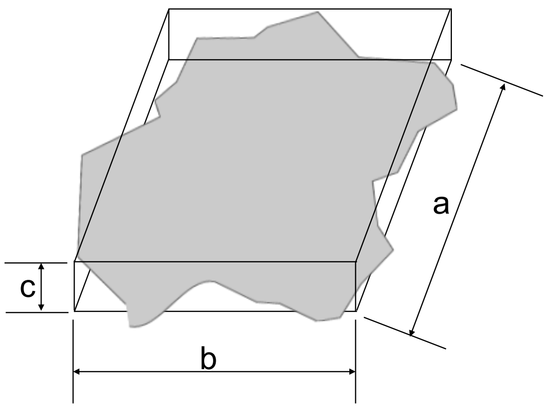

Figure 1.1: Approximation of a complex particle geometry by a cuboid (according to [1])

The edge lengths of the particles must be measured and can then be compared to each other. Figure 1.2 shows the measured aspect ratios of selected RDF fractions in a Zingg diagram. The figure shows the characteristic ranges for the fractions, but also the dispersion of particle geometries within the fractions. For this reason, the statistical distribution of particle geometries must also be taken into account, especially with regard to simulations

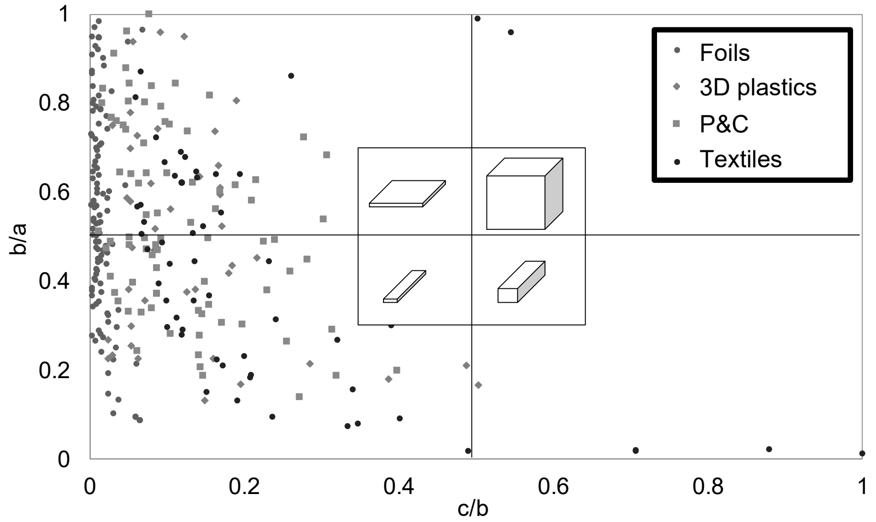

Figure 1.2: Zingg diagram of measured aspect ratios of some RDF fractions [1].

In a further step of the characterization, the particle mass must be determined. Based on the particle masses and the volumes of the cuboids, the resulting density of the fractions can be determined.

Using the average densities of the fractions, the equivalent diameters of the measured particles can be determined as follows:

$$d_V = \left(\frac{6\, m_p}{\pi \rho_{p,frac}}\right) \quad \text{Eq. 1.1}$$

Here, d_V is defined as the equivalent diameter of a volume-equivalent sphere, m_p denotes the particle mass, and $\rho_{p,frac}$ represents the mean density of the fraction. On the basis of the equivalent diameters, a Rosin–Rammler–Sperling–Bennett function (RRSB distribution) is employed to mathematically characterize the particle size distribution. The cumulative residue curve R is determined from the location parameter x' and the dispersion parameter n.

$$R(x) = e^{-\left(\frac{x}{x'}\right)^n} \quad \text{Eq. 1.2}$$

In comparison to conventional fuels, such as lignite dust with particle sizes in the micrometer range, alternative fuels exhibit significantly larger dimensions. Moreover, the actual edge lengths of the non-spherical RDF particles often exceed the calculated equivalent diameter by several multiples. From the RRSB distributions specified in the simulations, the principal edge length a can be back-calculated using the aspect ratios and the equivalent diameter.

$$a = d_V \cdot \sqrt[3]{\frac{\pi}{6} \cdot \left(\frac{a}{b}\right)^2 \cdot \frac{b}{c}} \qquad \text{Eq. 1.3}$$

1.2 Modeling of Combustion Behaviour

The RDF fractions can be classified into two groups. The first group comprises the biogenic fractions, such as cardboard, paper, and textiles, which exhibit combustion behaviour similar to fossil solid fuels through a pyrolysis process followed by a heterogeneous reaction of the remaining char. The second group includes the plastic fractions, whose conversion can be described by a phase transition from the solid to the liquid state, followed by thermal decomposition into the gas phase. Accordingly, the simulation model described below is based on the classification of refuse-derived fuel fractions into these two groups. The calculation is carried out in the CFD simulation separately for each fraction, according to the transformation mechanism assigned to its respective group.

Table 1.1 shows the allocation of the main fractions to the different groups and specifies the transformation processes considered in the modeling. For the biogenic, char-forming fractions, the modeling is conducted on the basis of established coal combustion models. For the plastic fractions, it is assumed that no residual char is formed, although this has been observed in individual particle reactor studies and in proximate analyses. The modeling of the plastic fractions follows the approach of a model for the thermal conversion of plastics introduced by Bluhm-Drehnhaus [2]. A particular feature is the change in particle geometry associated with the melting process, which affects not only the heat transfer but also the particle motion within the gas stream. For all fractions, it holds that the subprocesses listed in Table 1.1 can occur simultaneously within a single fuel particle.

Table 1.1: Transofrmation Phases considered in the Model and Allocation of the Fractions.

Conversion Process	Biogenic/char-forming fractions: **paper/cardboard (P&C), textiles, fines**	Synthetic fractions: **foils, 3D plastics**
I	Particle Heating	Particle Heating
II	Intra-Particle Drying	Surface Drying
III	Pyrolysis	Melting Process
IV	Char Combustion	Thermal Decomposition

1.2.1 Mass Balance of a Single Particle

The temporal change of the particle mass during thermal conversion is given by the sum of the changes of the fuel components: water (w), volatile matter (vol) and fixed carbon (C_{fix}).

$$\frac{\partial m_p}{\partial t} = \frac{\partial m_w}{\partial t} + \frac{\partial m_{vol}}{\partial t} + \frac{\partial m_{C_{fix}}}{\partial t} \qquad \text{Eq. 1.4}$$

For the plastic fractions, the fixed carbon fraction is assumed to be zero, and the corresponding mass fraction is assigned to the volatile components.

1.2.2 Particle Heating

The change in particle temperature is determined from the balance of heat fluxes around the single particle. The heat balance comprises, on the one hand, the heat exchange with the surroundings via convection and radiation and, on the other hand, the endothermic and exothermic thermochemical processes within the particle.

$$\frac{\partial Q_p(T_p(r,t))}{\partial t} = \sum\dot{Q} = \dot{Q}_{conv} + \dot{Q}_{rad} + \dot{Q}_{reac} \qquad \text{Eq. 1.5}$$

In the particle energy balance, $\dot{Q}_{conv}$ represents the heat flux transferred by convection, $\dot{Q}_{rad}$ the heat flux transferred by radiation, and $\dot{Q}_{reac}$ the resulting heat fluxes due to the transformation processes occurring within the particle, such as drying, pyrolysis, melting, and decomposition.

Convective Heat Flux

The magnitude of the heat transferred by convection is determined by the temperature difference between the gas stream and the particle surface $(T_g - T_{p,surf})$, the heat exchange area between the particle and the gas and the heat transfer coefficient α.

$$\dot{Q}_{conv} = \alpha\, A_p\left(T_g - T_{p,surf}\right) \qquad \text{Eq. 1.6}$$

The gas-exposed heat exchange area is equated here with the particle surface area A_P, which is calculated from the edge lengths of the cuboidal model particle. The heat transfer coefficient α is determined by the size and geometric proportions of the heat exchange area as well as the flow velocity. The heat transfer coefficient is estimated via the Nusselt number, taking into account the thermal conductivity of the gas λ_g and the characteristic length L_c.

$$\alpha = \frac{Nu\,\lambda_g}{L_c} \qquad \text{Eq. 1.7}$$

The Nusselt number is calculated by combining a turbulent and a laminar component [3] with a lower limit of 2.

$$Nu = 2 + \sqrt{Nu_{lam}^2 + Nu_{turb}^2} \qquad \text{Eq. 1.8}$$

The laminar and turbulent Nusselt numbers for the cuboidal particles assumed in the model are calculated using correlations for forced convection [4,5].

$$Nu_{lam} = 0{,}664\, {Re_p}^{1/2} Pr^{1/3} \qquad \text{Eq. 1.9}$$

$$Nu_{turb} = \frac{0{,}037 {Re_p}^{0,8}\, Pr}{1 + 2{,}443 {Re_p}^{-0,1}\, (Pr^{2/3} - 1)} \qquad \text{Eq. 1.10}$$

The dimensionless particle Reynolds number Re_P is calculated from the gas density ρ_G, the relative velocity between the gas and the particle $\vec{v}_p - \vec{v}_g$, the dynamic viscosity of the gas η_g and the characteristic length L_c.

$$Re_P = \frac{\rho_g \cdot |\vec{v}_p - \vec{v}_g| \cdot L_c}{\eta_g} \qquad \text{Eq. 1.11}$$

To determine the characteristic length of the refuse-derived fuel particles, a plate of length b of the particle is considered as being longitudinally exposed to the flow.

$$L_c = b = d_V \cdot \sqrt[3]{\frac{\pi}{6} \cdot \frac{b}{a} \cdot \frac{b}{c}} \qquad \text{Eq. 1.12}$$

Radiative Heat Flux

The radiative heat flux incident on the particle can be expressed for gray bodies using the Stefan–Boltzmann law as follows:

$$\dot{Q}_{rad} = \sigma \varepsilon_P A_p \left(T_{rad}^4 - T_{p,surf}^4\right) \qquad \text{Eq. 1.13}$$

The intensity of the radiative heat flux transferred is calculated from the difference between the fourth powers of the particle surface temperature and the effective radiation temperature T_{rad} of the surroundings, the particle surface area A_P, the particle emissivity ε_P and the Stefan–Boltzmann constant σ $(= 5{,}67040 \cdot 10^{-8}\, W\, m^{-2}\, K^{-4})$.

The effective radiation temperature is determined through the integration of the RDF model into the CFD software ANSYS Fluent® and is calculated there depending on the selected settings via the chosen radiation model (e.g. *Discrete-Ordinates-Model*). The CFD software calculates the intensity of the incident radiation G [W/m²] on the particle surfaces, treating the kiln walls as gray bodies. Furthermore, an overall gas emissivity is taken into account, which is calculated from the weighted sum of all gray gases according to the *Weighted-Sum-of-Gray-Gases Model* (*WSGGM*) by Hottel & Sarofim [6] with the weighting function of Smith [7]. The calculation of the overall emissivity also includes the local particle loading and their respective emissivities. The radiation temperature is then determined from the incident radiation as follows:

$$T_{rad} = \left(\frac{G}{4\sigma}\right)^{\frac{1}{4}} \qquad \text{Eq. 1.14}$$

Reaction Heat Fluxes

The chemical and physical processes occurring during the thermal conversion of the refuse-derived fuel particles generate additional heat sources or sinks within the particle, thereby affecting the heat balance. Depending on the transformation mechanisms assigned to the groups (Table 1.1) the heat flux for the biogenic, char-forming fractions results from drying (dry), pyrolysis (pyr) and heterogeneous char combustion ($char$)

$$\begin{aligned}\dot{Q}_{reac} &= \dot{Q}_{dry} + \dot{Q}_{pyr} + \dot{Q}_{char} \\ &= \frac{\partial m_w}{\partial t} \cdot \Delta h_w + \frac{\partial m_{vol}}{\partial t} \cdot \Delta h_{pyr} + \frac{\partial m_{C_{fix}}}{\partial t} \cdot \Delta h_{C_{fix}}\end{aligned} \qquad \text{Eq. 1.15}$$

and for the non-char-forming plastic fractions from drying (*dry*), the melting process (*melting*), and the decomposition of the molten material (*decomp*).

$$\begin{aligned}\dot{Q}_{reac} &= \dot{Q}_{dry} + \dot{Q}_{melting} + \dot{Q}_{decomp} \\ &= \frac{\partial m_w}{\partial t} \cdot \Delta h_w + \frac{\partial m_{solid}}{\partial t} \cdot \Delta h_{melting} + \frac{\partial m_{liquid}}{\partial t} \cdot \Delta h_{decomp}\end{aligned} \qquad \text{Eq. 1.16}$$

Internal Heat Transfer

For refuse-derived fuel particles, Biot numbers in the range of $Bi > 10$ occur, resulting in temperature gradients within the particle. For this reason, the refuse-derived fuel particles are discretized into 30 shells over the radius r in this work, and the one-dimensional heat conduction equation is numerically solved between the nodal points.

$$\frac{\partial T}{\partial t} = a_p \left(\frac{\partial^2 T}{\partial r^2} + \frac{n}{r}\frac{\partial T}{\partial r}\right) \qquad \text{Eq. 1.17}$$

In this equation, a_P denotes the thermal diffusivity of the particle. The solution of the one-dimensional heat conduction equation follows the approach of Brosch [8] , applying the Crank–Nicholson method [9] for a sphere ($n = 2$). This represents a certain simplification with respect to the initially rather flat RDF particles but significantly reduces the implementation effort, as the Discrete Phase Model always considers the diameter of a volume-equivalent sphere.

The application of the shell model enables the computational representation of the temperature distribution within the particle. In this way, reaction fronts for the conversion phases described later in this chapter can be calculated. These reaction fronts divide the particle into a region with a temperature above and a region with a temperature below a predefined threshold temperature and can thus determine the available masses that are assigned to the respective conversion phase. The reaction fronts are described by dimensionless reaction radii $r^+ = {r_T}/{r_p}$, which propagate from the particle surface toward the particle core.

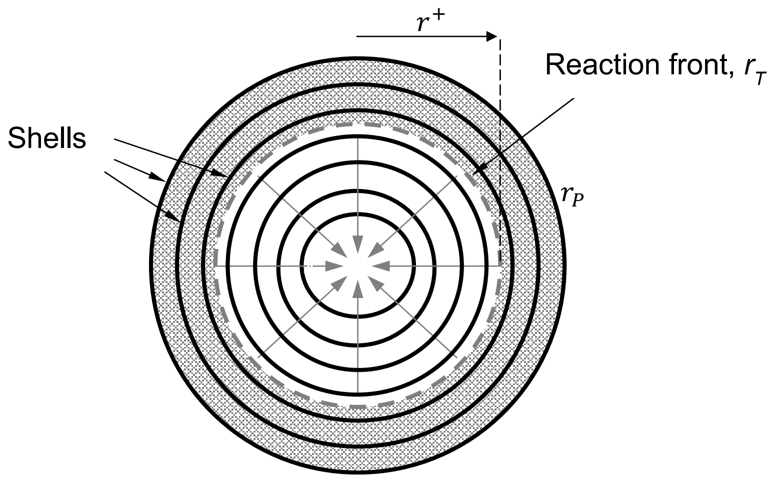

Figure 1.3: Progression of a Reaction Front in an RDF Particle [1].

Figure 1.3 illustrates the progression of a reaction front in a spherical particle. With increasing particle temperature, the reaction front advances from the particle surface ($r^+ = 1$) toward the particle core ($r^+ = 0$). The radius r_T represents the interpolated radius of an inner shell with a temperature above the defined reaction temperature. In contrast, the particle radius r_p always denotes the radius of the outermost nodal point and changes only in the case of a reduction in particle mass or size.

1.2.3 Drying

For the char-forming fractions, a uniform distribution of moisture within the porous and fibrous cell structures of the particles is assumed. Evaporation is therefore calculated via a dimensionless drying front inside the particle, along which temperatures of at least $T_{dry} = 100\ °C$ are present (intra-particle drying).

$$r_{Tr}^+ = \frac{r_{T>100°C}}{r_p} \qquad \text{Eq. 1.18}$$

Based on the drying front, the initial particle mass $m_{p,ini}$ and the initial water content Y_w, the maximum amount of water available for the subsequent drying process can be determined.

$$m_{w,max} = m_{p,ini} \cdot Y_w \cdot (1 - r_{Tr}^3) \qquad \text{Eq. 1.19}$$

For the plastic fractions, in contrast, it is assumed that the water is present only on the particle surface and that drying starts once the surface temperature exceeds 100 °C (surface drying). Due to the evaporation enthalpy of water Δh_W, the drying process requires additional heat for the phase transition of water into the gas phase. In the model, the total amount of heat transferred to the particle is therefore initially used for drying. Consequently, the available heat additionally limits the temporal change of the moisture content within or on the particle.

$$\frac{\partial m_w}{\partial t} = -\frac{\dot{Q}_{conv} + \dot{Q}_{rad}}{\Delta h_w} \qquad \text{Eq. 1.20}$$

This results, on the one hand, in a limitation of the drying process based on the transferred heat and, on the other hand, on the radial position of the drying front. Since the evaporation process leads to a reduction in particle mass, the model assumes a change in density while maintaining constant volume.

1.2.4 Pyrolysis

Since the pyrolysis rate of large particles depends both on heat transfer within the particle and on the chemical rate of the decomposition reactions, a combined modeling approach is employed. The limitation of the pyrolyzable mass m_{vol} is defined analogously to the drying model via a dimensionless pyrolysis radius r_{Pyr}^+, which describes the progression of a minimum pyrolysis temperature across the particle radius.

$$r_{Pyr}^+ = \frac{r_{T>T_{Pyr}}}{r_p} \qquad \text{Eq. 1.21}$$

The pyrolysis onset temperature was determined for paper/cardboard (C&P) and textiles using a LECO® TGA-601 under an inert gas atmosphere (N_2). From this, the reaction radius temperatures were derived as $T_{pyr,P\&C} = 240\ °C$ for P&C and $T_{pyr,Textiles} = 260\ °C$ for textiles.

The calculation of the volatile mass released during pyrolysis is performed using a multi-step reaction mechanism. This approach accounts for the macromolecular composition of the biogenic fractions and computes three independent parallel reactions for the main components: cellulose, hemicellulose, and lignin. The total released mass flow of the volatile components is thus obtained as the proportionate sum of the individual components.

$$\frac{\partial m_{vol}}{\partial t} = -\sum_{i} c_i \frac{\partial a_i}{\partial t} \qquad \text{Eq. 1.22}$$

Here, the coefficient c_i accounts for the respective fraction of the individual component in the total volatile mass. The reacted fraction a_i is calculated using a first-order Arrhenius approach.

$$\frac{\partial a_i}{\partial t} = k_{pyr_i} \cdot (1 - a_i) \qquad \text{Eq. 1.23}$$

with

$$k_{Pyr_i} = \frac{k_{0,pyr_i}}{V_p} \cdot \sum_{s} \exp\left(-\frac{E_{pyr_i}}{R \cdot T_{p,s}}\right) \cdot V_s \qquad \text{Eq. 1.24}$$

In Eq. 1.25 $k_{pyr,0_i}$ denotes the pre-exponential factor and E_{pyr_i} the activation energies of the respective reactions. Since the temperature distribution within the particle is known from the calculated heat conduction, the pyrolysis rate is computed for each shell at its respective temperature $T_{p,s}$. The pyrolysis rate is weighted by the volume V_s of the corresponding shell.

The selection of the kinetic parameters is based on the studies by Grammelis et al. [10] and Miranda et al. [11], which investigated the pyrolysis behaviour of various materials from processed refuse-derived fuels. Table 1.2 provides an overview of the chosen kinetic parameters for the P&C, textile, and fine fractions.

Table 1.2: Kinetic Data for the Pyrolysis of P&C and Textiles.

	Hemicellulose			**Cellulose**			**Lignin**		
	$k_{0,pyr}$ [1/s]	E_{pyr} [kJ/mol]	c [%]	$k_{0,pyr}$ [1/s]	E_{pyr} [kJ/mol]	c [%]	$k_{0,pyr}$ [1/s]	E_{pyr} [kJ/mol]	c [%]
C&P & Fines [10]	$1{,}35 \cdot 10^{9}$	116,3	27,2	$1{,}52 \cdot 10^{14}$	198,6	56,9	$5{,}00 \cdot 10^{-1}$	30,7	9,7
Textiles [11]	$8{,}33 \cdot 10^{1}$	41,0	24,0	$8{,}33 \cdot 10^{14}$	204,1	52,0	$1{,}66 \cdot 10^{11}$	180,0	14,2

The enthalpy of pyrolysis is assumed to be $\Delta h_{pyr} = 0 \frac{kJ}{kg}$. Analogous to the drying model presented in section 1.2.3, pyrolysis is also assumed to occur at constant volume with a simultaneous change in particle density.

1.2.5 Heterogeneous Char Combustion

Char combustion is modeled using a kinetic/diffusion-limited approach. An effective reaction rate for char combustion, $k_{C_{fix}}$, is calculated based on a chemical reaction rate k_c and a diffusion rate k_d. The rate of change of the char mass is thus determined from the effective reaction rate, the particle surface area, and the oxygen partial pressure in the gas phase $p_{O_2,g}$.

$$\frac{\partial m_{C_{fix}}}{\partial t} = -A_p \cdot p_{O_2,g} \cdot \frac{k_c \cdot k_d}{k_c + k_d} = -A_p \cdot p_{O_2,g} \cdot k_{C_{fix}} \quad \text{Eq. 1.26}$$

with

$$p_{O_2,g} = \frac{\rho_G R T_G Y_{O_2,g}}{M_{O_2}} \quad \text{Eq. 1.27}$$

The rate constant of the chemical reaction is formulated using an Arrhenius approach.

$$k_c = C_{1,C_{fix}} \cdot \exp\left[-\frac{E_{C_{fix}}}{RT_{p,surf}}\right] \quad \text{Eq. 1.28}$$

The constants used for the refuse-derived fuel fractions are again selected based on literature data [12] as $C_{1,c_{fix}} = 204 \cdot 10^{-5} \frac{kg}{m^2 s\ Pa}$ and $E_{c_{fix}} = 7{,}94 \cdot 10^{-5}\ J/mol$. The particle surface temperature $T_{p,surf}$ is taken as the temperature of the outermost shell.

The diffusion rate limits char combustion through the amount of oxygen transported to the particle surface.

$$k_d = \frac{C_{2,C_{fix}}}{2} \cdot Sh \cdot \Phi_{C_{fix}} \cdot \frac{\left[\left(T_{p,surf} + T_g\right)/2\right]^{0,75}}{d_V} \quad \text{Eq. 1.29}$$

with $C_{2,C_{fix}} = 5 \cdot 10^{-12} \frac{kg}{m \cdot s \cdot Pa \cdot K^{0,75}}$ [13].

The Sherwood number can be approximately expressed in terms of the Reynolds number and the Schmidt number [14].

$$Sh = 2 + 0{,}654\ \cdot Re_P^{\frac{1}{2}}\ \cdot Sc^{\frac{1}{3}} \quad \text{Eq. 1.30}$$

The Schmidt number is given by:

$$Sc = \frac{\eta_g}{\rho_g \cdot D_{O_2}} \quad \text{Eq. 1.31}$$

For the calculation of the diffusion coefficient D_{O_2}, the following correlation can be applied under the assumption of oxygen diffusion in a CO–N_2 mixture [15]:

$$D_{O_2} = D_{O_2,0} \cdot \frac{p_0}{p} \cdot \left(\frac{\left(T_{p,surf} + T_g\right)/2}{T_0}\right)^{1,75} \quad \text{Eq. 1.32}$$

with $D_{O_2,0} = 3{,}49 \cdot 10^{-4} \frac{m^2}{s}$, T_0 =1.327 °C and p_0 = 1 bar [12].

Since the particles are relatively large, the formation of CO from the heterogeneous reaction is neglected, and a direct conversion to CO_2 is assumed.

$$C + O_2 \rightarrow CO_2 \qquad \text{Eq. 1.33}$$

1.2.6 Melting Process

The modeling of the thermal conversion of the plastic fractions in this work is based on the assumption that all particles exhibit the behavior of thermoplastics. Once the particle temperature exceeds the melting temperature, a reversible transition of the particle mass into the liquid phase occurs [16]. The modeling approach assumes a total particle mass consisting of a solid (solid) and a molten (liquid) fraction.

$$m_p = m_{solid} + m_{liquid} \qquad \text{Eq. 1.34}$$

The phase transition within the particle is described, analogous to pyrolysis, by a dimensionless melting front propagating from the outside toward the center. The melting front determines the mass available for the melting process and is defined by exceeding a predefined melting temperature $T_{melting}$ along the particle radius.

$$r^+_{melting} = \frac{r_{T>T_{melting}}}{r_P} \qquad \text{Eq. 1.35}$$

The change in the solid mass is calculated from the progression of the melting front.

$$\frac{\partial m_{solid}}{\partial t} = -\rho_P \cdot \frac{\partial V_{solid}}{\partial t} = -\rho_P \cdot A_{boundary}\left(r^+_{melting}\right) \cdot \frac{\partial r^+_{melting}}{\partial t} \qquad \text{Eq. 1.36}$$

Here, $A_{boundary}$ denotes the phase interface at the melting front. The heat required for the endothermic melting process is calculated, taking into account the specific enthalpy of fusion $\Delta h_{melting}$, as follows:

$$\dot{Q}_{melting} = \frac{\partial m_{solid}}{\partial t} \cdot \Delta h_{melting} \qquad \text{Eq. 1.37}$$

The actual molten particle mass is additionally limited by the heat transferred to the particle in order to satisfy the energy balance (Eq. 1.5) for each time step. The values for the melting temperature and the specific enthalpy of fusion are assumed to be analogous to those of Bluhm-Drehnhaus [17] with $T_{melting} = 127\ °C$ and $\Delta h_{melting} = 150\ kJ/kg$.

During the melting process, the increase in the liquid fraction leads to a change in particle shape. Based on experimental results, linear functions are assumed for the geometry change of the 3D plastics and foils. These functions describe the change of the initial aspect ratios (*ini*) as a function of the melting radius once it exceeds a value of $r^+_{melting} = 0{,}5$. For the 3D plastic fraction, due to the relatively low initial aspect ratios:

$$a/_b = \frac{a/b_{ini} - 1{,}0}{0{,}5} \cdot r^+_{melting} + 1{,}0 \quad \text{Eq. 1.38}$$

$$a/_c = \frac{a/c_{ini} - 2{,}0}{0{,}5} \cdot r^+_{melting} + 2{,}0 \quad \text{Eq. 1.39}$$

and for the foils:

$$a/_b = \frac{a/b_{ini} - 1{,}5}{0{,}5} \cdot r^+_{melting} + 1{,}5 \quad \text{Eq. 1.40}$$

$$a/_c = \frac{a/c_{ini} - 8{,}0}{0{,}5} \cdot r^+_{melting} + 8{,}0 \quad \text{Eq. 1.41}$$

To illustrate the change in geometry, Figure 1.4 shows a particle of the 3D plastic fraction during the melting process. The change begins at a melting radius of $r^+_{melting} = 0{,}5$ and ends once the particle is fully molten ($r^+_{melting} = 0{,}0$). The initially flat particle shape (18.9 × 6.3 × 1.0 mm) transitions, according to the linear function (Eq. 1.38 – Eq. 1.39) into a body with more uniform edge lengths (6.1 × 6.1 × 3.1 mm).

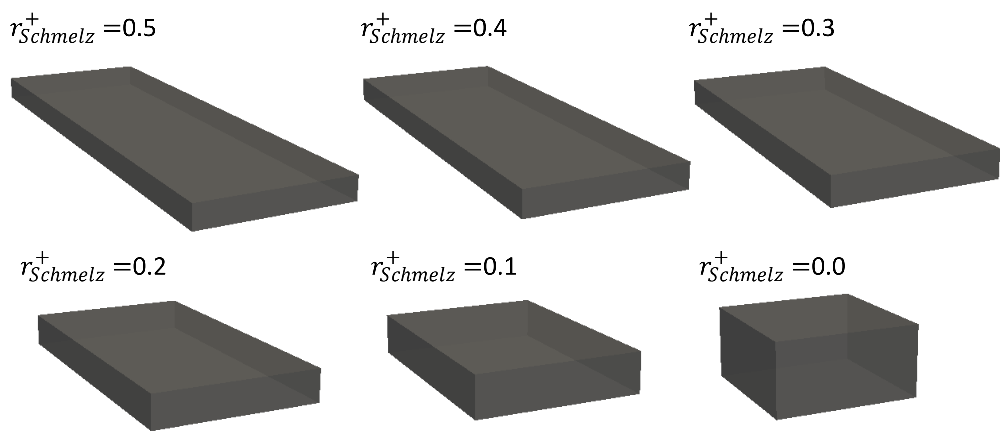

Figure 1.4: Change in Geometry of a 3D Plastic Particle during the Melting Process.

1.2.7 Thermal Decomposition

The mass change of the liquid phase within the particle is determined using a first-order Arrhenius approach with a temperature-dependent reaction rate.

$$\frac{\partial m_{liquid}}{\partial t} = -k_{decomp} \cdot m_{liquid} \quad \text{Eq. 1.42}$$

Analogous to the pyrolysis modeling, the decomposition rate is calculated for each shell at the corresponding local temperature and subsequently averaged over the particle volume.

$$k_{decomp} = \frac{k_{0,decomp}}{V_p} \cdot \sum_s \exp\left(-\frac{E_{decomp}}{R \cdot T_{p,s}}\right) \cdot V_s \qquad \text{Eq. 1.43}$$

The chosen kinetic parameters $k_{0,decomp} = 3{,}943 \cdot 10^{13}\ [1/s]$ and $E_{decomp} = 224{,}9\ kJ/mol$ were determined by Bluhm-Drehnhaus [17] for PE based on experimentally measured decomposition rates by Bockhorn et al. [18].

Since energy is required during thermal decomposition to break the chemical bonds of the polymers, it is an endothermic process. Therefore, the energy required for decomposition must be accounted for in the particle energy balance.

$$\dot{Q}_{decomp} = \frac{\partial m_{liquid}}{\partial t} \cdot h_{decomp} \qquad \text{Eq. 1.44}$$

The energy balance simultaneously limits, in addition to the reaction rate, the maximum mass that can be decomposed within a time step. For the specific enthalpy of decomposition, a value of $h_{decomp,25\,°C} = 230\ kJ/kg$ is used, analogous to Bluhm-Drehnhaus, assuming the decomposition of PE to dodecane ($C_{12}H_{26}$).

1.2.8 Chemical Reactions in the Gas Phase

The conversion of pyrolysis/decomposition gases in the gas phase is modeled using the Eddy-Dissipation Concept (EDC). In this approach, the transported gases react according to the following reaction scheme.

$$volatiles + v_1 O_2 \rightarrow v_2 CO_2 + v_3 H_2O + v_4 N_2 \qquad \text{Eq. 1.45}$$

In this approach, the composition of the released pyrolysis gases is calculated using pseudo-species $C_xH_yO_z$ based on the elemental and proximate analyses. Starting from the determined calorific values, the proximate analysis, and the calculated composition of the pseudo-species, a standard enthalpy of formation ΔH_f^0 is determined. The molar masses, standard enthalpies of formation, and the stoichiometric coefficients of the reaction equation for the volatile components of the individual RDF fractions are listed in Table 1.3.

For the calculation of the kinetically controlled conversion, a global kinetic approach according to Westbrook & Dryer [19] is employed, with $k_0 = 2{,}119 \cdot 10^{11}\ 1/s$ and $E = 2{,}027 \cdot 10^{8}\ kJ/mol$.

Table 1.3: Parameters for Gas-Phase Reactions of the Volatile Components of RDF Fractions (per mol of Volatiles).

Fraction	**M** $\left[\frac{g}{mol}\right]$	$\Delta H_f^0\ \left[\frac{J}{mol}\right]$	v_1	v_2	v_3	v_4
Fines	78,782	$-1.100697 \cdot 10^{6}$	4,398	3,269	4,117	0,052
Foils	100,000	$-2.578132 \cdot 10^{4}$	9,862	6,695	6,379	0,008

3D-Plastics	100,000	$-1.168794\cdot10^5$	9,122	6,521	5,819	0,002
P&C	83,564	$-5.793398\cdot10^5$	2,632	2,438	3,343	0,009
Textiles	88,435	$-5.153357\cdot10^5$	5,480	4,445	3,705	0,050

1.2.9 Consideration of the Statistics of RDF Properties

To account for the heterogeneity of refuse-derived fuels in simulations of industrial plants, additional particle properties can be assigned individually to each particle using statistically distributed random values, in addition to specifying an (RRSB) particle size distribution. The statistically assigned value P_i is calculated from a normally distributed random number ξ, the standard deviation σ_{P_i}, determined from the measurement data, and the arithmetic mean $\overline{P_\iota}$,.

$$P_i = \overline{P_\iota} + \xi \cdot \sigma_{P_i} \qquad \text{Eq. 1.46}$$

1.3 Modeling of Particle Motion

1.3.1 Model Fundamentals and Equations of Motion for Spherical Particles

In this work, the Discrete Phase Model (DPM) is used to describe both conventional (coal dust) and refuse-derived fuels. The DPM is based on the Euler–Lagrange approach for dispersed two-phase flows and calculates representative trajectories while accounting for the forces acting on the particles in the turbulent flow field.

The change in particle velocity $\vec{v}_p$ in the gas stream is calculated in the DPM by solving Newton’s equations of motion. For the coal dust particles and fine fraction particles considered as point masses in this work, the force balance of a single particle in gas–solid dispersions with low volume fraction and a large particle–fluid density difference reduces to:

$$m_p \frac{\partial \vec{v}_p}{\partial t} = \sum \vec{F} = \vec{F}_g + \vec{F}_D + \vec{F}_{L_{stat}} \qquad \text{Eq. 1.47}$$

Accordingly, only the gravitational force $\vec{F}_g$, the static buoyancy force $\vec{F}_{L_{stat}}$ and the drag force $\vec{F}_D$ are considered. The gravitational force (or weight) is the product of the particle mass m_p and the acceleration due to gravity $\vec{g}$.

$$\vec{F}_g = m_p \cdot \vec{g} \qquad \text{Eq. 1.48}$$

The resulting buoyancy force describes the displacement of the particle volume in a fluid and is determined from the ratio of the fluid density ρ_g to the solid density ρ_p.

$$\vec{F}_{L_{stat}} = m_p \cdot \vec{g} \cdot \frac{\rho_g}{\rho_p} \qquad \text{Eq. 1.49}$$

The drag force causes acceleration or deceleration of the particle parallel to the relative velocity vector $\vec{v}_p - \vec{v}_g$ due to frictional and form drag. The magnitude of the force depends on the particle's projected area $A_{p_\perp}$ in the direction of the relative velocity and a drag coefficient c_{drag}.

$$\vec{F}_D = \frac{1}{2} A_{p_\perp}\, \rho_g\, c_D \left|\vec{v}_p - \vec{v}_g\right| \cdot \vec{v}_p - \vec{v}_g \qquad \text{Eq. 1.50}$$

For the coal dust particles assumed to be spherical, the correlation by Schiller & Naumann [20] is used.

$$c_D = \begin{cases} 24\dfrac{1 + 0{,}15\, {Re_P}^{0{,}687}}{Re_P} & Re_P \leq 1000 \\ 0{,}44 & Re_P > 1000 \end{cases} \qquad \text{Eq. 1.51}$$

For the particle-related Reynolds number Re_P the equivalent diameter d_V is used as the characteristic length L_c.

$$Re_p = \frac{\rho_g \cdot \left|\vec{v}_p - \vec{v}_g\right| \cdot d_V}{\eta_g} \qquad \text{Eq. 1.52}$$

The modeling of the fine fraction is carried out by adjusting the drag coefficients according to the correlation of Haider & Levenspiel [21] for non-spherical particles.

$$c_D = \frac{24}{Re_p}\left(1 + b_1 \cdot Re_P^{b_2}\right) + \frac{b_3}{1 + \dfrac{b_4}{Re_p}} \qquad \text{Eq. 1.53}$$

With the coefficients $b_1 \ldots b_4$:

$$b_1 = e^{2{,}3288 - 6{,}4581\,\phi + 2{,}4486\,\phi^2} \qquad \text{Eq. 1.54}$$

$$b_2 = 0{,}0964 + 0{,}5565\,\phi \qquad \text{Eq. 1.55}$$

$$b_3 = e^{4{,}905 - 13{,}8944\,\phi + 18{,}4222\,\phi^2 - 10{,}2599\,\phi^3} \qquad \text{Eq. 1.56}$$

$$b_4 = e^{1{,}4681 + 12{,}2584\,\phi - 20{,}7322\,\phi^2 + 15{,}8855\,\phi^3} \qquad \text{Eq. 1.57}$$

The sphericity ϕ is defined as the ratio of the surface area of a volume-equivalent sphere A_V to the actual surface area of the non-spherical particle A_p.

$$\phi = \frac{A_V}{A_p} = \frac{\pi \cdot d_V^2}{2 \cdot (a \cdot b + a \cdot c + b \cdot c)} \quad \text{Eq. 1.58}$$

1.3.2 Extension of the Model for Describing the Motion of RDF

Coordinate systems and particle orientation

The particle motion depends on its orientation within the flow field. For this reason, the particle orientation must be continuously calculated. To describe the particle orientation, a global inertial system of the simulation environment $[x, y, z]$ and a local particle coordinate system $[x', y', z']$ with its origin at the geometric center of the particle are introduced. Additionally, a coordinate system $[x'', y'', z'']$ is defined, whose axes are parallel to the inertial system but are also located at the particle center and move with the particle. Figure 1.5 provides an overview of the coordinate systems and their orientations.

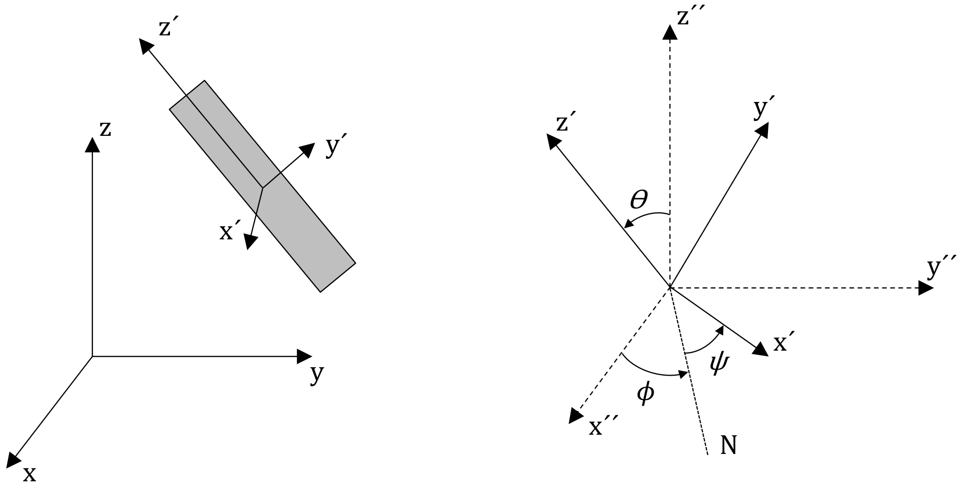

Figure 1.5: Definition of the coordinate systems and the Euler angles (adapted from [22]).

The rotation of the particle coordinate system relative to the inertial system can be described using three Euler angles (θ, ϕ, ψ). The rotation of the coordinate system follows a fixed sequence: first, a rotation by the angle ϕ around the z''-axis in the initial position; next, a rotation by the angle θ around the x'-axis in its position after the first rotation (N) and finally, a rotation by ψ around the z'-axis in its position after the first two rotations.

The transformation between the inertial and particle coordinate systems is performed using a transformation matrix A or its transpose A^T.

$$\vec{x} = A \cdot \vec{x}' \qquad \text{Eq. 1.59}$$

$$\vec{x}' = A^T \cdot \vec{x} \qquad \text{Eq. 1.60}$$

The transformation matrix A is obtained by multiplying the three rotation matrices of the Euler angles in three-dimensional space.

$$A = \begin{bmatrix} \cos\psi\cos\phi - \cos\theta\sin\phi\sin\psi & \cos\psi\sin\phi + \cos\theta\cos\phi\sin\psi & \sin\psi\sin\theta \\ -\sin\psi\cos\phi - \cos\theta\sin\phi\cos\psi & -\sin\psi\sin\phi + \cos\theta\cos\phi\cos\psi & \cos\psi\sin\theta \\ \sin\theta\sin\phi & -\sin\theta\cos\phi & \cos\theta \end{bmatrix} \qquad \text{Eq. 1.61}$$

The temporal change of the Euler angles is directly related to the angular velocities.

$$\begin{bmatrix} \frac{d\theta}{dt} \\ \frac{d\phi}{dt} \\ \frac{d\psi}{dt} \end{bmatrix} = \begin{bmatrix} \omega_{x'}\cos\psi - \omega_{y'}\cos\psi \\ (\omega_{x'}\sin\psi + \omega_{y'}\cos\psi)/\sin\theta \\ \omega_{z'} - (\frac{d\phi}{dt})\cos\theta \end{bmatrix} \qquad \text{Eq. 1.62}$$

Here, $[\omega_{x'}, \omega_{y'}, \omega_{z'}]$ are the angular velocities of the particle relative to the particle coordinate system. Instead of describing the rotation of the coordinate systems around three axes, the rotation can also be represented around a single axis in space. This allows the use of quaternions, in this case the Euler parameters according to Hughes [23] $\varepsilon_1, \varepsilon_2, \varepsilon_3$and η.

$$A = \begin{bmatrix} 1 - 2(\varepsilon_2^2 + \varepsilon_3^2) & 2(\varepsilon_1\varepsilon_2 + \varepsilon_3\eta) & 2(\varepsilon_1\varepsilon_3 - \varepsilon_2\eta) \\ 2(\varepsilon_2\varepsilon_1 - \varepsilon_3\eta) & 1 - 2(\varepsilon_3^2 + \varepsilon_1^2) & 2(\varepsilon_2\varepsilon_3 + \varepsilon_1\eta) \\ 2(\varepsilon_3\varepsilon_1 + \varepsilon_2\eta) & 2(\varepsilon_3\varepsilon_2 - \varepsilon_1\eta) & 1 - 2(\varepsilon_1^2 + \varepsilon_2^2) \end{bmatrix} \qquad \text{Eq. 1.63}$$

with

$$\varepsilon_1 = \cos\frac{\phi - \psi}{2}\sin\frac{\theta}{2}, \quad \varepsilon_2 = \sin\frac{\phi - \psi}{2}\sin\frac{\theta}{2}$$
$$\varepsilon_3 = \sin\frac{\phi + \psi}{2}\cos\frac{\theta}{2}, \quad \eta = \cos\frac{\phi + \psi}{2}\cos\frac{\theta}{2} \qquad \text{Eq. 1.64}$$

The Euler angles are used for the initial assignment of the particle orientation. Subsequently, for each time step dt, the change of the Euler parameters is calculated based on the angular velocities $[\omega_{x'}, \omega_{y'}, \omega_{z'}]$.

$$\begin{bmatrix} \frac{d\varepsilon_1}{dt} \\ \frac{d\varepsilon_2}{dt} \\ \frac{d\varepsilon_3}{dt} \\ \frac{d\eta}{dt} \end{bmatrix} = \frac{1}{2} \begin{bmatrix} \eta\omega_{x'} - \varepsilon_3\omega_{y'} + \varepsilon_2\omega_{z'} \\ \varepsilon_3\omega_{x'} + \eta\omega_{y'} - \varepsilon_1\omega_{z'} \\ -\varepsilon_2\omega_{x'} + \varepsilon_1\omega_{y'} + \eta\omega_{z'} \\ -\varepsilon_1\omega_{x'} - \varepsilon_2\omega_{y'} - \varepsilon_3\omega_{z'} \end{bmatrix} \qquad \text{Eq. 1.65}$$

Forces and moments on the particle

Figure 1.6 illustrates, in a two-dimensional view, the forces and moments acting on a cuboid particle in a uniform gas flow. Due to the relative velocity between the particle and the gas phase $\vec{v}_{rel}$ different pressure regions (+ high pressure, − low pressure) arise on the particle surface in the flow direction. Since the particle is not in its equilibrium position — i.e., the normal vector of the particle surface does not point in the direction of the relative velocity vector— the point of application P_D of the drag force and the dynamic lift force $\vec{F}_{L_{dyn}}$ is shifted relative to the center of mass P_m by a distance δ. In contrast, the gravitational force acts through the particle's center of mass, generating a moment $\vec{M}_1$ on the particle. This moment induces rotation of the particle about its center of mass.

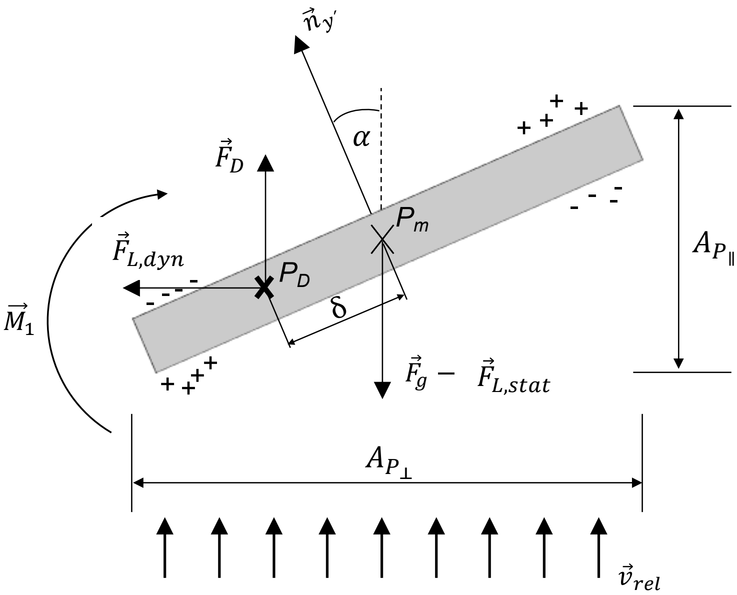

Figure 1.6: Forces and moments acting on a non-spherical particle in a uniform flow (after [24]).

The force balance (Eq. 1.47) is extended for the cuboid particle accordingly to include the dynamic component of the lift force.

$$m_P \frac{\partial \vec{v}_P}{\partial t} = \sum \vec{F} = \vec{F}_g + \vec{F}_D + \vec{F}_{L_{stat}} + \vec{F}_{L_{dyn}} \qquad \text{Eq. 1.66}$$

The dynamic lift force arises due to the pressure gradient on the particle surface generated by the particle's flow, and it always acts perpendicular to the drag force, or equivalently, to the direction of the incoming flow.

$$\vec{F}_{A_{dyn}} = \frac{1}{2} A_{P_\parallel} \, \rho_G \, c_L \, |\vec{v}_P - \vec{v}_G| \cdot \vec{v}_P - \vec{v}_G \qquad \text{Eq. 1.67}$$

The magnitude of the lift force is determined by the relative velocity, the area projected perpendicular to the flow direction $A_{P_\parallel}$, and the lift coefficient c_L, which is determined by the particle geometry.

The lift and drag coefficients for non-spherical bodies depend not only on the Reynolds number but also on the particle orientation in the flow, and they fluctuate accordingly during rotational motion. The drag and lift coefficients for complex aspherical particles are determined in a drop-tube experiment. The experimental values correspond to the Newtonian regime of the Reynolds number. Therefore, an adjustment for the Stokes and transitional regimes at Reynolds numbers <1000 is made using the equation according to Kaskas [25].

$$c'_D = \frac{24}{Re_P} + \frac{4}{\sqrt{Re_P}} + c_D \qquad \text{Eq. 1.68}$$

The drag coefficients determined from drop-tube experiments apply in simulations of industrial furnaces for fractions undergoing shape changes only to the initial state upon entry into the combustion chamber. This initial state is often of short duration, but it can decisively influence the subsequent trajectory due to the high impulses present at the burner outlet.

The shape change of certain fractions during combustion is described in more detail in section 1.2.6. Once a shape change occurs in the corresponding fractions, the drag coefficients derived from experimental statistical distributions are no longer used. Instead, the drag coefficients are calculated using the correlation of Hölzer & Sommerfeld [26] for non-spherical bodies. This empirical correlation accounts for the particle shape and orientation over the entire range of Reynolds numbers.

$$c_D = \frac{8}{Re_P} \cdot \frac{1}{\sqrt{\phi_\parallel}} + \frac{16}{Re_P} \cdot \frac{1}{\sqrt{\phi}} + \frac{3}{\sqrt{Re_P}} \cdot \frac{1}{\phi^{\frac{3}{4}}} + 0{,}42 \cdot 10^{0{,}4 \cdot (-\log \phi)^{0{,}2}} \frac{1}{\phi_\perp} \qquad \text{Eq. 1.69}$$

In this correlation, the longitudinal sphericity $\phi_\parallel$ denotes the ratio of the cross-sectional area of a volume-equivalent sphere to the difference between half the surface area and the area of the particle projected in the flow direction. The transverse sphericity $\phi_\perp$ is defined as the ratio of the cross-sectional area of a volume-equivalent sphere to the particle area projected perpendicular to the flow direction. The corresponding lift coefficient is estimated using the cross-flow principle according to Hoerner [27].

$$c_L = c_D \cdot \sin\alpha \cdot \cos\alpha^{\,2} \qquad \text{Eq. 1.70}$$

In the above equation, α denotes the angle between the normal vector of the particle surface and the flow direction. The underlying particle surface is determined from the particle length a and width b. For values of $\alpha \neq 0$ the center of pressure on the particle surface is shifted relative to the center of mass, inducing a torque.

To illustrate the lever arms of the acting forces, Figure 1.7 shows a three-dimensional view of a cuboid with the corresponding angles α, β, γ between the particle principal axes and the flow direction.

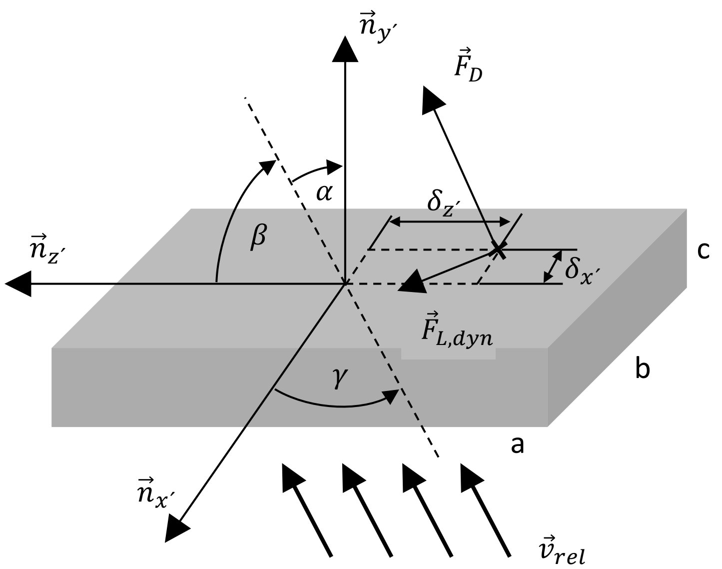

Figure 1.7: Definition of the angles and lever arms in the three-dimensional model.

The following equation is used to calculate the lever arm $\vec{\delta}$:

$$\vec{\delta} = 0.25 \cdot \begin{pmatrix} \mathrm{b} \cdot \cos\gamma^{\,3} \\ 0 \\ \mathrm{a} \cdot \cos\beta^{\,3} \end{pmatrix} \qquad \text{Eq. 1.71}$$

The lever arm along the particle height (side c) is not considered due to the flat particle geometry.

Consequently, the torque acting on the particle's center of mass is given by the cross product of the lever arm and the force vector.

$$\vec{M}_1 = \vec{\delta} \times (\vec{F}_D + \vec{F}_{L_{dyn}}) \qquad \text{Eq. 1.72}$$

With the approximation of the particle shape as a cuboid, the geometric center inevitably coincides with the center of mass. In real refuse-derived fuel particles, however, due to their complex geometry with varying thicknesses (e.g., partially folded foils), these two points are often offset. This results in an equilibrium position of the real particle that differs from the assumed equilibrium position of the cuboid ($\alpha = 0$). Consequently, a torque acts on the real particle even when the model particle would be in its equilibrium state. For this reason, an additional corrective moment $\vec{M}_2$ is calculated analogously.

$$\vec{M}_2 = \vec{\delta}_g \times \vec{F}_g \qquad \text{Eq. 1.73}$$

The vector $\vec{\delta}_g$ between the center of mass and the geometric center of the particle is also sampled from a normal distribution determined in the drop-tube experiments using a random number generator. Due to the angular acceleration induced by the torques, a resistive moment opposing the rotation also acts, which is derived from the flow resistance of a rotating cuboid.

$$M_{3,x'} = \frac{1}{64} \cdot c_D \cdot \rho_g \cdot b \cdot \vec{\omega}_x \cdot a^4 \qquad \text{Eq. 1.74}$$

$$M_{3,y'} = \frac{1}{64} \cdot c_D \cdot \rho_g \cdot c \cdot \vec{\omega}_y \cdot a^4 \qquad \text{Eq. 1.75}$$

$$M_{3,z'} = \frac{1}{64} \cdot c_D \cdot \rho_g \cdot a \cdot \vec{\omega}_z \cdot b^4 \qquad \text{Eq. 1.76}$$

Finally, the particle's mass moment of inertia must be taken into account. For a cuboid, this can be determined using the edge lengths parallel to the respective axis of rotation.

$$\mathrm{I}_{x'} = \frac{1}{12} \cdot \rho_p \cdot V_p \cdot (a^2 + c^2) \qquad \text{Eq. 1.77}$$

$$\mathrm{I}_{y'} = \frac{1}{12} \cdot \rho_p \cdot V_p \cdot (a^2 + b^2) \qquad \text{Eq. 1.78}$$

$$\mathrm{I}_{z'} = \frac{1}{12} \cdot \rho_p \cdot V_p \cdot (b^2 + c^2) \qquad \text{Eq. 1.79}$$

From the moment balance about the particle's center of mass, the change in angular velocities can be described using the Euler equations of motion.

$$\frac{\partial \omega_{x'}}{\partial t} = \frac{M_{1,x'} + M_{2,x'} + M_{3,x'} + \omega_{y'} \cdot \omega_{z'} (\mathrm{I}_{y'} - \mathrm{I}_{z'})}{\mathrm{I}_{x'}} \qquad \text{Eq. 1.80}$$

$$\frac{\partial \omega_{y'}}{\partial t} = \frac{M_{1,y'} + M_{2,y'} + M_{3,y'} + \omega_{x'} \cdot \omega_{z'} (\mathrm{I}_{z'} - \mathrm{I}_{x'})}{\mathrm{I}_{y'}} \qquad \text{Eq. 1.81}$$

$$\frac{\partial \omega_{z'}}{\partial t} = \frac{M_{1,z'} + M_{2,z'} + M_{3,z'} + \omega_{y'} \cdot \omega_{x'} (\mathrm{I}_{x'} - \mathrm{I}_{y'})}{\mathrm{I}_{z'}} \qquad \text{Eq. 1.82}$$

2 References

[1] **Liedmann B., Arnold W., Krüger B., Becker A., Krusch S., Wirtz S. et al.:** *An approach to model the thermal conversion and flight behaviour of Refuse Derived Fuel*, Fuel, Vol. 200, DOI: 10.1016/j.fuel.2017.03.069, 2017.

[2] **Bluhm-Drenhaus T., Becker A., Wirtz S., Scherer V.:** *A model for the devolatilisation of large thermoplastic particles under co-firing conditions*, Fuel, Vol. 101, pp. 161–170, DOI: 10.1016/j.fuel.2012.05.041, 2012.

[3] **Verein Deutscher Ingenieure VDI-Gesellschaft Verfahrenstechnik und Chemie-ingenieurwesen (GVC):** *VDI-Wärmeatlas*, 10. ed., Springer Berlin, Heidelberg, Düsseldorf, ISBN: 9783540255048, 2006.

[4] **Pohlhausen E.:** *Der Wärmeaustausch zwischen festen Körpern und Flüssigkeiten mit kleiner reibung und kleiner Wärmeleitung*, ZAMM - Zeitschrift Für Angewandte Mathematik Und Mechanik, Vol. 1 (2), pp. 115–121, DOI: 10.1002/zamm.19210010205, 1921.

[5] **Gnielinski V.:** *Berechnung mittlerer Wärme- und Stoffübergangskoeffizienten an laminar und turbulent überströmten Einzelkörpern mit Hilfe einer einheitlichen Gleichung*, Forschung Im Ingenieurwesen, Vol. 41 (5), pp. 145–153, DOI: 10.1007/BF02560793, 1975.

[6] **Hottel H.C., Sarofim A.F.:** *Radiative Transfer*, McGraw-Hill, New York, 1967.

[7] **Smith T.F., Shen Z.F., Friedman J.N.:** *Evaluation of Coefficients for the Weighted Sum of Gray Gases Model*, Journal of Heat Transfer, Vol. 104 (4), pp. 602–608, DOI: 10.1115/1.3245174, 1982.

[8] **Brosch B.:** *Erweiterung der Diskreten Elemente Methode zur Simulation bewegter und reagierender Feststoffschüttungen mit der Anwendung auf Rostfeuerungssysteme*, Dissertation, Ruhr-Universität Bochum, 2012.

[9] **Crank J., Nicolson P.:** *A practical method for numerical evaluation of solutions of partial differential equations of the heat-conduction type*, Advances in Computational Mathematics, Vol. 6 (1), pp. 207–226, DOI: 10.1007/BF02127704, 1996.

[10] **Grammelis P., Basinas P., Malliopoulou A., Sakellaropoulos G.:** *Pyrolysis kinetics and combustion characteristics of waste recovered fuels*, Fuel, Vol. 88 (1), pp. 195–205, DOI: 10.1016/j.fuel.2008.02.002, 2009.

[11] **Miranda R., Sosa-Blanco C., Bustos-Martínez D., Vasile C.:** *Pyrolysis of textile wastes. I. Kinetics and yields*, Journal of Analytical and Applied Pyrolysis, Vol. 80 (2), pp. 489–495, DOI: 10.1016/j.jaap.2007.03.008, 2007.

[12] **Görner K.:** *Technische Verbrennungssysteme - Grundlagen, Modellbildung, Simulation*, Springer-Verlag, Berlin, Heidelberg, 1991.

[13] **Wall, T.F., Phelan, W.J., Bartz S.:** *The Prediction and Scaling of Burn-out in Swirled Pulverized Coal Flames: An Analysis and Mathematical Modelling of the AP11, AP12 and AP13 Trials*, IJmuiden, The Netherland, 1986.

[14] **Smoot L.D., Pratt D.T., editors:** *Pulverized-Coal Combustion and Gasification*, Springer US, Boston, MA, ISBN: 978-1-4757-1698-6, 1979.

[15] **Zelkowski J.:** *Kohlecharakterisierung und Kohleverbrennung*, 2. Ed. ed., VGB TowerTech e.V., Essen, ISBN: 978-3-86875-216-8, 2004.

[16] **Ruge J., Wohlfahrt H.:** *Technologie der Werkstoffe*, Springer Fachmedien Wiesbaden, Wiesbaden, ISBN: 978-3-658-01880-1, 2013.

[17] **Bluhm-Drenhaus T.:** *Numerische Simulation der thermischen Zersetzung von Kunststoffen am Beispiel von Ersatzbrennstoffen in Calcinatoren der Zementindustrie*, Dissertation, Ruhr-Universität Bochum, 2011.

[18] **Beyler C.L., Hirschler M.M.:** *Thermal Decomposition of Polymers*, SPE Handbook of Fire Protection Engineering, pp. 110–131, DOI: 10.1021/cm200949v, 2001.

[19] **Dryer F.L., Westbrook C.K.:** *Simplified Reaction Mechanisms for the Oxidation of Hydrocarbon Fuels in Flames*, Combustion Science and Technology, Vol. 27 (1–2), pp. 31–43, DOI: 10.1080/00102208108946970, 1981.

[20] **Schiller L., Naumann A.:** *A drag coefficient correlation*, Zeitschrift Des Vereins Deutscher Ingenieure, Vol. 77, pp. 318–320, 1935.

[21] **Haider A., Levenspiel O.:** *Drag Coefficient and Terminal Velocity of Spherical and Nonspherical Particles*, Powder Technology, Vol. 58, pp. 63–70, 1989.

[22] **Goldstein H., Poole C., Safko J., Addison S.R.:** *Classical Mechanics, 3rd ed.*, American Journal of Physics, Vol. 70 (7), pp. 782–783, DOI: 10.1119/1.1484149, 2002.

[23] **Hughes P.C.:** *Spacecraft Attitude Dynamics*, Wiley, New York, ISBN: 978-0486439259, 1986.

[24] **Krüger B.:** *Experimentelle Charakterisierung und Modellierung der Flugbewegung von asphärischen Partikeln*, Dissertation, Ruhr-Universität Bochum, 2016.

[25] **Kaskas A.:** *Scharmgeschwindigkeiten in Mehrkornsuspensionen am Beispiel der Sedimentation*, Dissertation, TU Berlin, 1970.

[26] **Hölzer A., Sommerfeld M.:** *New simple correlation formula for the drag coefficient of non-spherical particles*, Powder Technology, Vol. 184 (3), pp. 361–365, DOI: 10.1016/j.powtec.2007.08.021, 2008.

[27] **Hoerner S.F.:** *Fluid-Dynamic Drag*, Hoerner Fluid Dynamics, Bricktown, New Jersey, ISBN: 9993623938, 1965.

Appendix

Table A1: Properties of the fuels used.

	Einheit	3D	Foils	P&C	Textiles	Fines	Total
Composition	[m.-%]	25,70	30,50	11,70	10,20	21,90	100
H_O (wf)	[MJ/kg]	40,69	39,79	15,96	23,58	16,06	30,38
H_U (roh)	[MJ/kg]	37,79	36,72	10,78	20,61	10,22	26,51
Proximate analysis (raw)							
Water	[m.-%]	1,05	0,95	25,68	6,26	28,48	10,44
Ash	[m.-%]	1,04	5,09	10,68	10,99	17,51	8,03
Fix Carbon	[m.-%]	0,00	0,00	10,46	9,57	11,46	4,71
Volatiles, average	[m.-%]	97,91	93,96	53,19	73,18	42,55	76,83
Volatiles, Std. Dev. (σ)	[m.-%]	2,44	2,86	2,56	3,05	13,90	-
Ultimate analysis (waf)							
C	[m.-%]	78,93	80,42	45,72	64,96	60,48	66,88
H	[m.-%]	12,03	12,86	6,74	7,47	8,30	9,85
N	[m.-%]	0,07	0,22	0,24	1,39	1,47	0,62
O	[m.-%]	8,98	6,50	47,30	26,18	29,75	22,65
RRSB (Standard)							
$d_{v,max}$	[m]	1,27E-02	8,30E-03	1,48E-02	9,28E-03	3,00E-03	-
$d_{v,min}$	[m]	3,30E-03	1,48E-03	1,39E-03	1,82E-03	3,00E-04	-
$d_{v,mittel}$	[m]	9,40E-03	4,60E-03	7,70E-03	6,30E-03	1,56E-03	-
N	[-]	5,11	3,27	3,57	2,96	2,19	-
RRSB (fine)							
$d_{v,max}$	[m]	1,02E-02	6,70E-03	9,00E-03	7,77E-03	2,00E-03	-
$d_{v,min}$	[m]	2,90E-03	1,40E-03	2,00E-03	1,60E-03	3,00E-04	-
$d_{v,mittel}$	[m]	7,50E-03	3,80E-03	5,60E-03	4,80E-03	1,30E-03	-
N	[-]	4,76	3,65	3,89	3,61	2,19	-
Geometry							
a/b_{mittel}	[-]	2,73	2,86	2,25	4,63	2,55	-
a/b_{σ}	[-]	1,63	2,94	1,16	11,20	1,20	-
a/c_{mittel}	[-]	34,80	202,00	29,83	19,40	14,86	-
a/c_{σ}	[-]	40,20	161,1	25,81	15,67	3,86	-
further Parameters							
Density	[kg/m³]	812	822	640	362	800	-
Heat conductivity	[W/m/K]	0,35	0,35	0,10	0,08	0,31	-
Spez. Heat capacity	[J/kg/K]	1.900	1.900	1.258	1.325	1.844	-
Emissivity	[-]	0,80	0,80	0,85	0,85	0,85	